Article

A novel mechanobiological model of bone metastasis reveals that mechanical stimulation inhibits the pro-osteoclastogenic effects of breast cancer cells

Vatsal Kumar[1#], Syeda M. Naqvi[1#], Anneke Verbruggen[1], Eoin McEvoy[2] and Laoise M. McNamara[1*]

[1] Mechanobiology and Medical Device Research Group (MMDRG), University of Galway, Ireland.
[2] Biomedical Engineering, College of Science and Engineering, University of Galway, Ireland.

[#] Both authors contributed to this manuscript equally
[*] Corresponding Author

Abstract:
Tumor metastasis into bone alters the biomechanical cues experienced by both tumor and native bone cells (osteoblasts, osteoclasts and osteocytes). Both bone and tumor cells are regulated by mechanical stimuli, yet the mechanobiological role bone and tumor cells play in driving osteolysis are not yet fully understood. Here, 3D in vitro co-culture and computational models were developed to investigate the coupled influence of tumor-bone cell signaling and growth induced matrix stress on tumor growth. We also developed advanced in vitro 3D models of the in vivo multicellular and mechanical environment and confirmed the ability of this model to recapitulate osteoblast, osteoclast and metastatic activity. We applied this bone metastasis model to investigate how interactions between tumor and bone cells, and their surrounding biophysical environment dictate osteolysis and tumor development. Our results revealed that tumor spheroid growth is regulated by the synergistic influence of bone cell signaling and matrix stiffness. We also demonstrate for the first time the importance of mechanical loading in attenuating breast cancer cell activity and signaling for osteoclastogenesis during early stage bone metastasis.

1. Introduction

Bone metastasis occurs when primary tumor cells spread from their site of origin and invade bone tissue, where they form osteolytic or osteoblastic lesions[1]. Bone is highly targeted by breast cancer and it has been shown that osteoblasts express chemokines (CXCL12/SDF-1α), which facilitate homing of tumor cells to bone[2]. During osteolytic metastasis tumor cells produce factors, such as parathyroid hormone-related protein (PTHrP), matrix metallopeptidases (MMPs), interleukins (IL-6, IL-8, IL-11) and vascular endothelial growth factor (VEGF)), which stimulate osteoclasts to actively degrade bone matrix[3]. These factors also stimulate osteoblasts to secrete RANKL, which further stimulates osteoclast resorption of bone matrix. This resorption results in a release of growth factors stored in the mineralized matrix, such as transforming growth factor β (TGF-β) or Insulin-like growth factors (IGFs), which stimulate tumor cell proliferation and further release of growth factors that perpetuates tumor and bone cell activity[3]. In this way, tumor cells and bone cells interact to enable tumor invasion and growth into bone tissue as part of a complex process known as the 'vicious cycle'[4,5]. Although much research has been conducted to understand the pathogenesis of metastatic bone disease, it remains that therapies are deficient and once cancer invades bone tissue the condition is widely untreatable and accounts for 90% of cancer deaths worldwide[6]. Thus, there is a distinct need to significantly advance our scientific understanding of bone metastasis.

Many cells are intricately governed by the mechanical stimuli arising in their environment. Within bone, the coordinated activities of osteocytes, osteoblasts and osteoclasts govern structure and composition and elicit biochemical signaling to other cells (mechanotransduction) when this environment is not favorable. Mechanobiological factors have been implicated in breast cancer, in particular tumor growth, invasion, homing and metastasis[7-14]. Within the primary tumor, changes in the composition of the extracellular matrix occur, which alter the biophysical environment[15] and can promote proliferation and transition of tumor cells to migrating cells[10-12,16-20]. Indeed, it has been demonstrated that MDA-MB-231 breast cancer cells cultured on stiff substrates (3 kPa) increased proliferation compared to those cultured on soft substrates (0.6 kPa)[21]. Furthermore, PTHrP expression is upregulated by MDA-MB-231 cells with increasing substrate rigidity (2000 to 365,000 kPa), promoting the progression of the tumor cells from the pre-osteolytic to the osteolytic phase and formation of bone metastasis[22]. As they evolve, metastatic bone tumors become less stiff compared to non-tumor bone tissue[23,24] and the presence of the tumor likely alters the biophysical cues acting on the bone cells, through the exertion of tumor pressure and by altering matrix stiffness. Given the well-established relationship between matrix properties, mechanical stimuli and bone biology, such changes may activate mechanobiological responses in both native bone cells, and also tumor cells, perpetuating the "vicious cycle" driving bone lysis and tumor growth. However, how the coupled mechanobiological responses of tumor and bone cells contributes to osteolysis and tumor growth is not understood.

Much of our understanding of metastasis comes from animal models [25-30], in which the normal responses of the immune system are suppressed, or in vitro 2D cell culture studies, which cannot represent the complex in vivo environment because of the loss of native morphology and interactions with the surrounding matrix[31]. More recently, three-dimensional (3D) in vitro tumor models have been developed to study the invasion of breast cancer cells into bone samples from patients undergoing total hip replacement[32,33]. A recent experimental model used bioprinted calcium phosphate coated polycaprolactone scaffolds cellularized with human osteoprogenitor cells, which were then seeded with human prostate cancer cells[34] to study response to androgen-targeted therapy. They reported that cancer/bone stroma interactions and anti-androgens drive cancer progression in a mineralized microenvironment. Another study fabricated a metastatic bone model by encapsulating osteoblasts, osteoclasts, bone-resident macrophages, endothelial cells and breast cancer cells in a fibrin hydrogel[35], and showed organ-tropism of breast cancer cells towards bone and compared this to a simplified metastatic muscle model in which the proliferation of breast cancer cells was significantly lower. Another study used a 3D printed biocompatible resin (DS3000) scaffold conditioned with osteoblast-like cells, a collagen matrix, and mineralized calcium, to which patient-derived xenografted metastatic breast cancer cells were added[36]. This study demonstrated that the cancer cells colonized the scaffold and exhibited a modulated sensitivity to chemotherapy drugs. A more recent study developed bone-like scaffolds, using either collagen matrices with controlled intrafibrillar mineral deposition or decellularized bone scaffolds, and showed the

importance of matrix mineralization in early stage bone metastasis[37]. Specifically, they reported that higher levels of mineral led to quiescence through a reduction in mechanosignalling. More recently, a 3D in vitro tumor model was developed to study the invasion of 4T1 murine mammary carcinoma cells. encapsulated in gelatin-transglutaminase (mtgase) hydrogels of different substrate stiffness (1 or 2.7 kPa)[38]. To understand the influence of mechanical stimuli on tumor growth, a custom bioreactor was used to apply cyclic mechanical compression (1 hour/day for 4 days) [38]. The results of this study revealed that tumor spheroid growth was restricted in stiffer and mechanically compressed hydrogels[38]. Moreover, mechanical compression has been reported to inhibit tumor growth through reduced osteolysis in immunocompromised SCID mice, and in vitro, in poly(lactide-co-glycolide) (PLG) and hydroxyapatite (HA) scaffolds seeded with MDA-MB-231 cells[39]. It has also been shown that compression can suppress tumor induced osteolysis in vivo[40]. However, the role of mechanical stimulation in the bone environment on the development of osteolytic bone metastases is not yet fully understood. To address this question requires advanced experimental models that can replicate both (1) the complex multicellular niche (osteoblasts, osteoclasts, osteocytes, tumor cells) and (2) the native mechanical environment that exist in-vivo. [40].

The global objective of this research is to develop an advanced *ex-vivo* model that can provide an effective surrogate of the in vivo environment to investigate the coupled influence of tumor cell-bone cell signalling and growth-induced matrix stress on tumor spheroid evolution and osteoclast activity. The first specific objective was to (1) study the growth-induced matrix stress on tumor spheroid evolution by developing a 3D in-vitro model and a novel computational model of tumor spheroid growth. The in-vitro model was then extended to (2) include bone cells to study the coupled influence of tumor cell-bone cell signaling on tumor spheroid evolution. The final objective was to (3) develop a 3D in vitro multicellular (osteoblasts, osteocytes, osteoclasts, breast cancer cells) and mineralised bone metastasis model incorporating mechanical loading using a custom designed bioreactor. We applied this advanced *ex-vivo* model model of bone metastasis to study how mechanical compression can inhibit osteolytic activity within these mimetic models.

2. Results

2.1 Tumor spheroid growth is stress dependent

Multicellular spheroids are a promising experimental model for in vivo tumor growth, but the biomechanical factors regulating such growth in a three-dimensional (3D) environment remain unclear. To investigate the mechanoregulation of spheroid expansion, we encapsulated 4T1 breast cancer cells in a monoculture configuration within gelatin-transglutaminase hydrogels of varying compression modulus, reflective of the mechanical properties of bone marrow [41] (Figure 1a). We monitored spheroid development over 7 days, starting from single cells, and observed that the rate of spheroid growth reduced with increasing gel stiffness (Figure 1b). We thus characterized the number of cells per spheroid, and indeed found that the number of cells was higher in softer hydrogels (Figure 1b).

To investigate whether cell proliferation was stress-dependent, we also developed a computational model to characterize mechanosensitive growth. We considered that the proliferation of tumor cells (c_t) was dependent on spheroid stress ($\boldsymbol{\sigma}$) induced by hydrogel deformation, such that

$$\frac{\mathrm{dc_t}}{\mathrm{dt}} = \left(\frac{\mathrm{c_t}}{\tau_\mathrm{t}}\right)(1 - \mathrm{tr}(\boldsymbol{\sigma})/(3p_0)), \tag{1}$$

where τ_t is the timescale for tumor proliferation in the absence of other factors and p_0 is the reference pressure for mitotic inhibition. To simulate growth we adopted a multiplicative decomposition of the deformation gradient $\mathbf{F}$ into $\mathbf{F_g}$ (growth tensor) and $\mathbf{F_e}$ (elastic tensor)[42,43], such that $\mathbf{F} = \mathbf{F_e}\mathbf{F_g}$. Here, $\mathbf{F_g} = \lambda_\mathrm{g}\mathbf{I}$, where $\lambda_\mathrm{g} = (\mathrm{c_t}/\mathrm{c_0})^{1/3}$ is the growth stretch, $\mathbf{I}$ is the second order identity tensor and c_0 is the initial number of cells in a spheroid. Simulations revealed that the increased circumferential and radial stresses generated by spheroid expansion in a stiffer microenvironment can reduce the rate of cell proliferation, in agreement with our experimental observations (Figure 1d, 1e). Having established that 4T1 spheroid growth is stress-dependent, we proceeded to explore the coupled influence of hydrogel stiffness and bone cell signaling on in vitro tumor development.

2.2 Osteoclasts have an inhibitory effect on tumor spheroid growth which is partially alleviated by osteoblasts

To study the coupled effect of individual bone cells on tumor spheroid growth, RAW264.7 osteoclast precursors and MC3T3-E1 osteoblast-like cells were encapsulated within separate gelatin-transglutaminase hydrogel suspensions and cultured in different culture configurations with 4T1 cells for 7 days: mono-culture (4T1), co-culture (RAW264.7 + 4T1, MC3T3 + 4T1) and tri-culture (MC3T3 + RAW264.7 + 4T1 (Figure 2a).

When co-cultured with MC3T3 cells, the size of the 4T1 tumor spheroids was significantly lower relative to those that were formed in the 4T1 monoculture, but only in the 0.58 kPa hydrogels. However, when co-cultured with RAW264.7 cells, the tumor spheroids were significantly smaller than the ones formed in monoculture in 0.58 kPa, 0.85 kPa and 1.1 kPa hydrogels (Figure 2d). This reduction in spheroid size in co-culture with RAW264.7 cells was partially mitigated by the inclusion of MC3T3 cells (i.e. in the tri-culture group) in 0.58 and 0.85 kPa hydrogels (Figure 2d).

We carried out Quantitative Real Time PCR (qRT-PCR) to analyze mRNA expression of genes implicated in the growth of tumor cells (TGF-β) and biochemical signaling between the cancer and bone cells (TNF-α, IL-6 and PTHrP). ***Tumour growth:*** Transforming growth factor beta (TGF-β) was significantly downregulated, compared to the 4T1 monoculture, in the 0.85 kPa tri-culture group and the 1.1 kPa RAW264.7 co-culture group (Figure 2e). ***Tumour-bone cell signaling:*** Tumor necrosis factor alpha (TNF-α) mRNA expression was significantly upregulated, when compared to the 4T1 monoculture, in the 0.58 kPa and 0.85 kPa tri-culture groups (Figure 2f). Furthermore, TNF-α expression was upregulated in the 0.58 kPa RAW264.7 co-culture group compared to the 4T1 monoculture, albeit this was not statistically significant ($p = 0.0657$) (Figure 2f). Interestingly, TNF-α expression was significantly lower in the 0.58 kPa MC3T3 co-culture group compared to RAW264.7 encapsulated co-culture and the tri-culture groups for the same stiffness (Figure 2f). Moreover, TNF-α expression was significantly lower for the 0.85 kPa MC3T3 co-culture group compared to the 0.85 kPa tri-culture group (Figure 2f). We report a significant upregulation in Interleukin 6 (IL-6) mRNA expression for the 0.85 kPa and 1.1 kPa MC3T3 co-culture groups compared to the 4T1 monoculture (Figure 2g). Expression of IL-6 was higher in the 0.58 kPa and 1.1 kPa MC3T3 co-culture groups compared to the RAW264.7 co-culture groups (Figure 2g). A similar trend was evident for the 0.85 kPa MC3T3 co-culture group compared to the 0.85 kPa RAW264.7 co-culture group, albeit this was not statistically significant ($p = 0.0647$) (Figure 2g). PTHrP expression was higher in the 1.1 kPa RAW264.7 co-culture group compared to the 0.58 kPa RAW264.7 co-culture group (Figure 2h). For the MC3T3 co-culture group, there was higher expression of PTHrP in the 1.1 kPa hydrogels when compared to 0.85 kPa hydrogels (Figure 2h).

2.3 Development of a Bone Multicellular Model: presence of mineral deposits and active osteoclasts

In vivo, multiple bone cells reside within a 3D niche and are embedded in a mineralized matrix, where they interact biochemically and experience mechanical loads. Interestingly, a recent study showed that mineralization (1) alters breast cancer cell gene expression and growth in vitro (2) increases a stem-like phenotype in breast cancer cells and (3) regulates breast cancer cell phenotype by altering mechanosignaling[37]. Thus, to more closely mimic the in vivo physiological and mechanical environment, bone multicellular (BM) models were fabricated by (1) developing mineralized hydrogels by culturing OCY 454 and MC3T3-E1 cells within gelatin-mtgase hydrogels in osteogenic media for 21 days, to which (2) murine RAW264.7 osteoclast precursor cells encapsulated in gelatin-mtgase hydrogels were added onto these mineralized constructs and (3) subjecting these models to mechanical stimulation using a custom built compression bioreactor (0.5% strain, 1 hour per day for 7 days) see Figure 3a. Constructs under static conditions served as controls.

Our results confirmed the development of a mineralized 3D bone-multicellular model under both static and stimulated conditions, as confirmed by micro-CT scanning at both day 24 and day 28 (Figure 3b). Biochemical analyses reveal an increase in calcium content in the mechanically stimulated BM model compared to static controls at day 24, and no significant difference between stimulated and static groups at day 28 (Figure 3c). A significant decrease in calcium content was observed in the stimulated groups at day 28 compared to day 24. By micro-CT analysis, no change in mineral volume (BV/TV) was evident between static and stimulated groups at day 24 or day 28 (Figure 3d). However, by day 28, BM models had developed significantly

more high-density mineral content (M_{high}) than at day 24, both in the static and stimulated groups (Figure 3e). Under static conditions there is a significant increase in full width at half max (FWHM) at day 28 compared to day 24 (Figure 3f).

Quantitative real time PCR (qRT-PCR) revealed that mechanical stimulation upregulated osteogenic genes. Specifically, bone sialoprotein (BSP2 – intermediate osteoblast marker) mRNA expression was upregulated in mechanically stimulated groups compared to static controls at day 24 (Figure 3g). Osteopontin (OPN – early osteoblast marker) and dentin matrix acidic phosphoprotein 1 (DMP1 – late osteoblast marker) mRNA expression was upregulated in mechanically stimulated groups compared to static controls at day 28 (Figure 3h and 3i), whereas BSP2 mRNA expression was downregulated in mechanically stimulated groups compared to static controls at day 28 (Figure 3g).

There was a significant increase in pro-osteoclastogenic gene expression (RANKL (receptor activator of NF-κβ ligand): OPG (Osteoprotegerin) ratio) in mechanically stimulated BM models at day 24 compared to static controls (Figure 3j). In contrast to day 24 results, there was a significant decrease in RANKL:OPG gene expression in mechanically stimulated BM models at day 28 compared to static controls (Figure 3j). This in keeping with the known inhibitory effect of mechanical loading on bone resorption[44,45]

Immunofluorescence and histology for Cathepsin-K (CTSK), Tartrate Resistant Acid Phosphatase (TRAP) and Haemotoxylin and Eosin (H&E) confirmed the differentiation of osteoclast precursors to multinucleated active osteoclasts (nuclei > 3) (CTSK and TRAP positive) osteoclasts in the in mineralized bone-like multicellular 3D models (BM model) at day 24 and day 28 under both mechanically stimulated and static conditions (Figure 3k). Nuclear Factor of Activated T Cells 1 (NFATC1) and Osteoclast-associated receptor (OSCAR) mRNA expression was significantly upregulated under mechanical stimulation in the BM model when compared to static controls at day 28 (Figure 3l and 3m). There was no detectable difference in IL-6 and Avβ3 immunofluorescence staining between the static and stimulated groups (Figure 3n).

2.4 Metastatic Multicellular model exhibit osteolytic response

To mimic the physiological and mechanical environment of bone metastasis in vivo, metastatic multicellular (MM) models were fabricated by layering murine RAW264.7 and 4T1 breast cancer cell encapsulated gelatin-transglutaminase onto previously mineralized hydrogels (approach described above), which were then subjected to mechanical stimulation at 0.5% strain for 1 hour per day using a custom built compression bioreactor for 7 days (Figure 4a and 5a). Constructs under static conditions served as controls. We confirmed cancerous behavior of the MM model based on increased cancer cell activity (PTHRP mRNA expression and IL-6 immunostaining). We also confirmed the metastatic behavior of the MM model based on reduced osteoblast activity, increased osteoclastogenesis and pro-osteoclastogenic gene expression.

Paracrine signaling for osteoclastogenesis (RANKL:OPG ratio) was significantly higher ($p \leq 0.05$) for the metastatic multicellular (MM) model (day 24: 0.57 ± 0.05; day 28: 3.05 ± 0.14) compared to the BM model (day 24: 0.03 ± 0.05; day 28: 0.62 ± 0.05) under static conditions (Figure 3j, 4l and 5a). Moreover, OSCAR mRNA expression was significantly upregulated ($p \leq 0.05$) in the MM model (406.62 ± 10.54) at day 28 compared to the BM model (4.39 ± 0.11) under static conditions (Figure 3m, 4m and 5a). Furthermore, IL-6 staining and PTHrP mRNA expression were notably increased in the MM model under static conditions (7.65 ± 0.41) at day 28, compared to the BM model (0.55 ± 0.46), see Figures 3n, 4k, 4o and 5a. These results are in keeping with the known osteolytic nature of 4T1 breast cancer cells and confirms the models ability to recapitulate the osteolytic metastatic process.

BSP2 mRNA expression was significantly downregulated ($p \leq 0.05$) in the presence of 4T1 breast cancer cells (1741.87 ± 80.92) compared to BM model (9703.13 ± 60.72) by day 28, suggesting reduced osteoblast activity in the MM model (Figure 3g, 4h and 5a). Under static conditions, there was significantly ($p \leq 0.05$) more high-density mineral in the MM models (MHigh 8.88 ± 0.102) compared to BM model (MHigh 0.3 ± 0.104) by day 24, but no significant difference by day 28 (Figure 3e and 4f). Furthermore, static MM models (FWHM 426.36 ± 23.86) were significantly ($p \leq 0.05$) more heterogeneous at day 24 compared to static BM models (FWHM 172.52 ± 1.34), but not at day 28 (Figure 3f and 4g). Mineral heterogeneity may be an indicator of bone quality[46], and has been previously reported in osteolytic bone tissue from pre-clinical animal

models of breast cancer metastasis[47,48] as well as in trabecular bone tissue in the femoral heads of osteoporotic and diabetic patients[49].

2.5 Osteolytic metastatic response is attenuated under mechanical compression

Osteoclast marker OSCAR mRNA expression was significantly upregulated in the mechanically stimulated MM model at day 24 compared to static controls, however, there was a significant downregulation of OSCAR under stimulation at day 28 (Figure 4m and 5b), when compared to static controls. Most interestingly, mechanical stimulation resulted in a reduction in RANKL/OPG expression in the MM models at both day 24 and day 28, when compared to static controls (Figure 4l and 5b). Furthermore, mRNA expression of PTHrP and immunostaining for IL-6 were significantly downregulated/decreased in the mechanically stimulated MM model, when compared to static control at day 28 (Figure 4k, 4o and 5b).

ALP activity increased in the mechanically stimulated MM models compared to the static controls at day 24 (Figure 4c). By day 28, there was no significant difference in ALP activity and calcium content between static and stimulated models (Figure 4c and 4d). MicroCT data confirmed that there was reduced bone mineral volume fraction in the mechanically stimulated MM models compared to the static controls at day 24 (Figure 4b and 4e). Mineral volume fraction was reduced by day 28 compared to day 24 in the static MM models. However, a significantly larger % of mineral was high in density (MHigh) in the mechanically stimulated MM models, compared to MM static controls by day 28 (Figure 4f).

Quantitative RT-PCR indicated downregulation in BSP2 mRNA expression at day 24 and an upregulation at day 28 in the MM models in response to mechanical stimulation, when compared to static controls (Figure 4h and 5b). DMP1 and SOST mRNA expression were significantly upregulated in the mechanically stimulated MM model compared to static controls, at both time points for DMP1 and at day 24 for SOST (Figure 4i, 4j and 5b). A similar upregulation in DMP1 mRNA expression was evident at day 28 (Figure 4i). However, SOST mRNA expression at day 28 was downregulated in response to mechanical stimulation compared to static controls (Figure 4j).

3. Discussion

Bone is subjected to unique physical and biomechanical conditions that are not easily replicated in vitro, but biomaterial-based models are a step closer to achieving more accurate models for studying bone pathology. Here we sought to develop an advanced an advanced *ex-vivo* model that could serve as an effective surrogate for the in vivo environment for studies of tumor cell-bone cell signalling, tumor spheroid evolution and osteoclast activity. We firstly cultured 4T1 breast CCs within gelatin-mtgase hydrogels and investigated the influence of matrix stiffness on tumor spheroid growth. Simultaneously we developed a novel computational model to characterize the stress sensitivity of the growth of these tumor spheroids. Next, we co-cultured bone cells with breast cancer cells and investigated the coupled influence of matrix stiffness and tumor cell-bone cell signaling on tumor spheroid growth. Our results reveal for the first time a synergistic influence of osteoclasts, osteoblasts and 3D matrix stiffness on tumor spheroid growth. We further developed a 3D mineralized bone multicellular (BM) model and applied extrinsic mechanical compression using a custom-built compression bioreactor to recreate the multicellular and mechanical environment in vivo. Next, we developed a metastatic multicellular (MM) model, which recreated the typical pro-osteoclastogenic effect of breast cancer cells under static conditions, and investigated how mechanical stimulation influenced osteoclast activity and metastasis. Altogether, this study provides advanced in vitro 3D multicellular experimental and computational models for studying the coupled influence of growth induced matrix stress and tumor cell-bone cell signaling on tumor spheroid growth during metastasis. The results of this study highlight the importance of mechanical loading for inducing breast cancer cell signaling to inhibit osteoclastogenesis and osteoblast activity in early stage bone metastasis.

This study has a number of limitations that must be considered. Firstly, there are inherent limitations in using cell lines for our studies, which may behave differently in terms of cell-cell signaling and mechanobloigcal responses than primary cells. However, it was not possible to complete the study with all human cells, because of potential difficulties arising in terms of isolating sufficient cells for the multiple different cell

types and inter-patient variability, and our experiments included mouse bone and mouse cancer cells, so that the potential effects of cross-species interactions did not influence our study. Another limitation is that immune and endothelial cells were not included, which are present in vivo and may play an additional role in influencing tumor and bone cell activity during metastasis. However, this study did enable us to study specific bone-tumor cell signaling without the complexity of additional cell influences. Thirdly, this study incorporated only compression stimulus, and cannot account for other mechanical stimuli, such as perfusion, that may play an important role in stimulating bone and tumor cells in vivo. However, the mechanical stimulus (0.5% compressive strain) was chosen to induce osteogenic differentiation[50] and would also be expected to induce some perfusion due to the movement of fluid through the nanoscale porosity of the gelatin hydrogel. Lastly, these models are not fully representative of in vivo bone, in terms of the extent of mineral deposition and stiffness (16.203 +/- 0.089 kPa), which is of the order of ~0.5-25 GPa. However, it is important to note that the stiffness of our gels increased 27 fold from at day 0 (0.58 kPa) so substantial mineralization of the 3D models in this study was achieved.

Our computational model simulations and experimental analysis confirm that tumor cell proliferation is stress dependent, but more importantly we show for the first time that the co-culture of 4T1 cells with osteoblasts or osteoclast precursors further reduced tumor spheroid size. Significant reductions in tumor spheroid size in co-culture with osteoclast precursors could be attributed to the expression of TNF-α and TGF-β1, both factors known to be secreted by the RAW264.7 cells[51,52], which have previously been linked to reduced tumor growth [53-55]. Indeed, in this study we observe significant differences in TNF-α expression such that we have an upregulation in the osteoclast precursor co-culture and tri-culture groups only. Interestingly, we observed increases in tumor spheroid size when in co-culture with osteoblasts compared to RAW264.7 co-culture and tri-culture groups. In this study we observed an upregulation of IL-6 in the osteoblast co-culture group compared to RAW264.7 co-culture and tri-culture groups. Thus osteoblasts might regulate spheroid growth through their expression of IL-6, which has been shown to suppress osteoclastogenesis of precursor cells, which may in-turn affect production of TGF-β[56].

This study confirms the development of a novel mineralized 3D bone-like multicellular model, which was shown to be well mineralised and expressed known osteogenic markers. Despite an increase in calcium content in the mechanically stimulated bone-like model compared to static controls at day 24, calcium content appeared to be similar for bone-like models cultured with and without mechanical stimulation at day 28. This is in contrast to a previous study in our laboratory, which demonstrated that the application of mechanical stimulation resulted in increased mineralization in osteoblast-only encapsulated hydrogels in vitro[57]. In other studies, mechanical stimulation of osteoblasts has been shown to activate specific signaling pathways[58], which stimulate the production of anabolic growth factors and synthesis of extracellular matrix proteins and mineral[59]. In fact, dynamic compression can promote the differentiation and mineralization of both osteoblasts and stem cells toward osteogenesis both in vitro and in vivo[60-64]. It may be that here the inclusion of others cells in the multicellular niche suppressed the typical induction of mineral production by osteoblasts cultured in isolation under mechanical stimulation. In particular, the inclusion of osteoclasts may have inhibited mineral production by signaling to osteoblasts. Of relevance, semaphorin 4D produced by osteoclasts inhibits bone formation[65] in a manner similar to that of OPG, which also limits the osteoclast-promoting actions of RANKL. In this study, OPG was significantly upregulated in the mechanically stimulated bone-like model compared to the static controls. Another explanation may be that the active osteoclasts degraded the mineral during the timeframe of the study. Indeed, RANKL:OPG ratio and gene expression of osteoclast markers NFATC1 and OSCAR were significantly greater in the mechanically stimulated bone-like groups compared to static.

The results from this study further confirm the development of a novel 3D bone metastatic-like model. PTHrP is a known growth factor secreted by tumor cells, that plays an important role in the 'vicious cycle' cascade of events by stimulating the expression of RANKL by osteoblasts and osteocytes leading to osteoclast formation and ultimately bone loss[66]. Moreover, IL6 has been shown to enhance osteoclastogenesis by upregulating RANKL in osteocytic MLO-Y4 cells[67]. We report that PTHrP and OSCAR gene expression and fluorescence intensity for IL-6 and CTSK were all upregulated or increased significantly for the bone metastatic-

like model under static conditions. These results are in keeping with the known osteolytic nature of 4T1 breast cancer cells and confirms the model's ability to recapitulate the osteolytic metastatic process [68]. Furthermore, these results confirm the differentiation of osteoclast precursors to active multinucleated osteoclasts in the metastatic model.

Mechanical stimulation reduced bone volume fraction, gene expression of PTHrP, pro-osteoclastogenic signaling (RANKL/OPG ratio) and IL-6 staining in the metastatic model. It has been demonstrated that the anti-catabolic effects of mechanical loading are modulated by nitric oxide (NO). Mechanical stimulation stimulates the release of NO from bone cells [69,70], and NO induces a decrease in the RANKL/OPG ratio. Although active osteoclasts were present in the mechanically stimulated metastatic model, there was a significant downregulation of OSCAR at day 28, compared to static controls. These results confirm the differentiation of osteoclast precursors to multinucleated active osteoclasts in the mineralized multicellular 3D models. Of importance, addition of osteoclast precursors to the 3D mineralized model, induced their differentiation into osteoclasts for both the bone-like multicellular and metastatic models without the need of an externally added cytokine to stimulate osteoclastogenesis, e.g. RANKL. In this way, we demonstrate the potential for these primed mineralized models (cultured in osteogenic growth factors) to be used in subsequent studies involving the use of osteoclast precursors.

4. Conclusions

This study provides an advanced 3D in vitro model for studying bone biology and metastasis, which recapitultates mineralisation, mechanical loading, osteoclast differentiation and tumor spheroid growth. This study provides an advanced understanding of how tumor growth and osteolysis are regulated by the evolving mechanical environment during tumor invasion of the bone. Using novel experimental and computational tumor growth models we showed for the first time, a synergistic influence of osteoclasts, osteoblasts and 3D matrix stiffness on tumor spheroid growth. By developing an advanced biomimetic 3D in vitro mineralized bone multicellular model, we successfully captured the osteolytic-metastatic process. This study reveals the importance of mechanical loading in attenuating breast cancer cell activity and signaling for osteoclastogenesis during early stage bone metastasis. This model will be used in the future to study how inhibition of mechanobiological responses can attenuate tumor cell-bone cell signaling and the development of osteolytic bone metastases.

5. Materials and Methods

5.1 Expansion of cells

Murine OCY454 osteocytic cells (Centre for Skeletal Research Bone Cell Core, an NIH-funded program (P30AR075042), which is supported by NIAMS) were expanded on type I collagen (0.15 mg/ml in 0.02 M acetic acid) coated T-175 flasks in standard growth media (α-MEM supplemented with 10% FBS, 100 U/mL penicillin, 100 μg/mL streptomycin and 2 mM L-glutamine) at the permissive temperature of 33°C in a humidified 5% CO_2 environment. The OCY454 cells were differentiated on T-175 flasks at the semi-permissive temperature of 37°C for 14 days in a humidified 5% CO_2 environment. Murine MC3T3-E1 osteoblastic cells (ATCC, Manassas, VA, USA) were expanded in standard growth media and maintained at 37°C in a humidified 5% CO_2 environment. Murine RAW264.7 osteoclast precursors (ATCC, Manassas, VA, USA) were expanded in their growth media (low glucose DMEM supplemented with 10% FBS (HyClone), 100 U/mL penicillin, 100 μg/mL streptomycin and 2 mM L-glutamine) and maintained at 37°C in a humidified 5% CO_2 environment. Murine mammary carcinoma 4T1 cells were expanded in their growth media (Roswell Park Memorial Institute (RPMI) supplemented with 10% FBS, 100 U/mL penicillin and 100 μg/mL streptomycin) and maintained at 37°C in a humidified 5% CO_2 environment. Cell culture media was replenished every 3 days.

5.2 Three-dimensional (3D) Static Culture

Cell encapsulating gelatin hydrogels of 3 different stiffness (0.58 kPa, 0.85 kPa ,1.1 kPa) were developed by crosslinking equal volumes of 9% cell laden gelatin and nano-Hydroxyapatite (nHa) (5.5% v/v) with sterile microbial transglutaminase (mtgase) containing Activa WM (Aginomoto Foods) of different concentrations

(0.3%, 0.6%, 1% w/w). These hydrogels had 4T1 breast CCs, MC3T3-E1 osteoblast-like cells, and RAW264.7 osteoclast-precursors in separate layers in various culture configurations (Monoculture:4T1, Co-culture: RAW+4T1, MC3T3+4T1, Tri-culture: MC3T3+RAW+4T1). The cell number was kept at 100,000 cells/hydrogel layer (2×10^6 cells/mL of hydrogel). All groups were cultured for 7 days (Fig. 1A) and assessed for tumor spheroid size (Actin, Nucleus), cell number (DNA) and proteins implicated in tumor cell- bone cell signaling: PTHrP, IL-6, TGF-β and TNF-α.

5.3 Fabrication of Bilayered models for mineralization

OCY454 cells were suspended in gelatin with an initial concentration of 9%. This cell suspension was enzymatically cross-linked with mtgase and with nHA (1:1:1 ratio), to yield a final gelatin concentration of 3% w/v, a mtgase concentration of 0.3% w/w of gelatin, a nHA concentration of 5.5% v/v, and an OCY454 cell density of 2×10^6 cells/mL. To fabricate the OCY454 layer this suspension was then pipetted into custom-made polydimethylsiloxane (PDMS) wells (1.33 mm × 6 mm D × 13 mm) and allowed to cool at 4°C for 8 min. Next, an MC3T3 gelatin/nHA suspension was crosslinked with mtgase as described for OCY454 cells. This suspension was pipetted on top of the OCY454 layer and allowed to cool at 4°C for 8 min to form an osteoblast layer (1.33 mm × 6 mm D × 13 mm). These bilayered models were cultured in standard growth media (α-MEM, 10% FBS, 100 U/mL penicillin, 100 μg/mL streptomycin, 2 mM L-glutamine) supplemented with osteogenic factors (50 μM ascorbic acid, 10 mM β-glycerophosphate, and 100 nM dexamethasone). Media was replenished every 3 days during a culture period of 21 days to allow for mineralization to occur.

5.4 Fabrication of bone multicellular (BM) and metastatic multicellular (MM) models

To fabricate the bone multicellular (BM) model, RAW264.7 encapsulated gelatin/nHA was enzymatically cross-linked with mtgase as described earlier. This suspension was pipetted on top of the osteoblast layer of the bilayered models, which had been cultured for 21 days as described in 2.2 above. These were allowed to cool at 4°C for 8 min.

To fabricate the metastatic multicellular (MM) model, RAW264.7 and 4T1 (1:1) encapsulated gelatin/nHA was enzymatically cross-linked with mtgase as described earlier. This suspension was pipetted on top of the osteoblast layer of the bilayered models. These were allowed to cool at 4°C for 8 min. These models were cultured as follows: (1) Bone Multicellular (BM): RAW 264.7 growth media and MC3T3/OCY454 growth media mixed at a ratio of 1:2 or (2) Metastatic Multicellular (MM): RAW 264.7 growth media, 4T1 growth media and MC3T3/OCY454 growth media mixed in a ratio of 1:1:2. Media was replenished every 3 days for the culture period to allow for proliferation and differentiation of the pre-osteoclasts and adenocarcinoma cells (7 days).

5.5 Mechanical Stimulation

Models from each experimental group were transferred from well plates to a sterile custom bioreactor (VizStim) containing their respective media, as described above. Four models were placed within each bioreactor chamber. The models were subjected to compression at 0.5 % strain for 1 hour per day for 7 days. At day 3 and day 7, the models were removed from culture and cut into quarters in both the sagittal plane and the transverse plane. These quarters were then processed for biochemical, histological, immunofluorescence, micro-computed tomography and PCR analyses. Static control groups were also included for all experimental conditions.

5.6 Biochemical Analyses

5.6.1 DNA Assay

DNA content was measured at each time point. Models were washed twice with phosphate buffered saline (PBS), weighed and then stored at -80°C. Models were then thawed and digested with 3.88 U/mL papain in 0.1 M sodium acetate, 5 mM L-cysteine-HCl, 0.05 M EDTA, pH 6.0 at 60°C under constant rotation for 18 h. DNA content was evaluated using the Hoechst 33258 DNA assay as previously described [71].

5.6.2 Extracellular ALP activity

Culture medium was collected for each experimental group and analyzed for ALP secreted into the media. At each time point models were maintained in an incubator for 2 hours, after the last bout of mechanical stimulation, before media was removed and stored at -80°C. ALP activity was determined using a colorimetric assay

of enzyme activity (SIGMAFAST p-NPP Kit), which uses p-nitrophenyl phosphate (pNPP) (nmol) as a phosphatase substrate, with ALP enzyme as a standard. After thawing, 40 µL of the medium was added to a 96-well plate in triplicate with a 50 µL of pNPP solution. The plate was shielded from direct light at room temperature for one hour. Colorimetric readings were taken at 405 nm using a microplate reader (Synergy HT Multi-mode), and converted to ALP activity by creating a standard ALP curve. ALP production was also normalised to DNA content to establish whether changes in mineralization were related to the overall mineral capacity of individual cells.

5.6.3 Mineralization

Calcium content within models was determined using a Calcium Liquicolour kit (Stanbio Laboratories, Syntec, Ireland) according to the manufacturer's protocol. At each time point, models were washed twice with PBS, weighed and stored at -80°C. Models were then thawed and digested by adding 1 mL of 1M hydrochloric acid (HCl) to each model and maintained at 60°C under constant rotation for 18 h. For each of the digested models and assay standards 10 µL was added to a 96-well plate and 200 µL of the working solution was added. The plate was read using a microplate reader at an absorbance of 550 nm, as previously described[72].

5.7 Histology

At each time point samples from each group were fixed in 4% paraformaldehyde (PFA) overnight, equilibrated in 30% sucrose solution, embedded in OCT embedding medium (VWR), sectioned at 20µm using a Cryostat (CM1850, Leica) and affixed to microscope slides (Fisher Scientific). The sections were stored at -20°C. Sections were then allowed to thaw and rinsed with PBS. Sections were stained with Haematoxylin and Eosin (H&E) and TRAP (all Sigma Aldrich). For H&E, sections were immersed in Mayer's Hematoxylin, before being immersed in running tap water. Slides were immersed three times in HCl/ethanol solution (1% HCl in 70% ethanol) before being stained with Eosin (Thermo scientific) for 3 minutes. Slides were then washed again with several deionised water rinses. Of note, only cells with 3 nuclei or more were considered to be osteoclasts. For TRAP, sections were rinsed with deionised water and stained for TRAP activity using a commercial kit and counterstained with Mayer's Hematoxylin for 10 seconds before being immersed in running tap water. All sections were allowed to completely air dry before mounting with DPX. Images were acquired using a light microscope (BX 43 Olympus Microscope, software cellSens).

5.8 Immunofluorescent Staining

Samples from each experimental group were stained for Actin, DAPI, cathepsin K (CTSK), Interleukin-6 (IL-6) and AVβ3. At 3 and 7 days of culture samples were fixed using 4% paraformaldehyde at 4°C overnight. Cells within the samples were permeabilized with 0.5% Triton-X in PBS for 10 min at 4°C under agitation. For staining the actin cytoskeleton and nucleus, the samples were stained with phalloidin-FITC at 1.25 µg/mL (1:400) and DAPI dilactate (1:2000), respectively.

For CTSK staining, the samples were immersed in 1% BSA blocking solution for 1h under agitation. Then these samples were incubated in Alexa Fluor 488 conjugated mouse monoclonal anti-CTSK antibody (1:100) at 4°C overnight (Merck) and then for 1h under agitation at room temperature. Samples were further counterstained with DAPI dilactate (1:2000) to stain the nucleus. For IL6, samples were incubated in goat polyclonal IL-6 antibody (Santa Cruz) (1:100) at 4°C overnight. After three washing steps in 1% BSA, the samples were incubated with Donkey anti goat Alexa 647 (Jackson ImmunoResearch) for 1 hour under agitation at room temperature. Integrin αvβ3 staining was carried out using an anti-αvβ3 antibody directly conjugated to Alexa Fluor® 488 (1:100) (Santa Cruz). Samples were further counterstained with DAPI dilactate (1:2000) and rinsed again with 1% BSA solution.

To quantify all immunofluorescent staining, Z-stack imaging was carried out using a Fluoview FV1000 confocal laser scanning microscope system (Olympus) at a magnification of 20x (oil) with a step size of 5 µm. All stacks were obtained at the same intensity setting between groups. NIH ImageJ software was used to analyze overall fluorescence intensity from combined stacks of images at maximum intensity projections. All fluorescent intensities were measured using the integrated density of each cell with their corresponding background integrated density subtracted.

5.9 Micro-Computed Tomography (µCT)

Samples from each experimental group were fixed using 4% paraformaldehyde at 4°C overnight for micro-computed tomography (μCT). Samples from each static and mechanically stimulated group were analyzed for mineralization by μCT scanning (Scanco Medical μCT100) using the following profile: 9 mm holder, 45 kVp tube voltage, 200 μA intensity, Al filter, 5 μm voxel size, 300 ms integration time, and a frame averaging value of 2. Samples were scanned in air and paper strips were used to minimize movement within the chamber. A density threshold of 370 mg HA/cm3 (3964 Hounsfield units) was applied to exclude hydrogel material and include mineralized regions, according to previously published work [57]. A volume of interest (VOI) of 3.95 mm^3 was segmented using Scanco Medical software (Switzerland) and evaluated for mineralization properties such as bone-like mineral volume fraction (BV/TV), bone mineral density distribution (BMDD) including mineral quantity which lies below the 25th percentile (M_{low}) or above the 75th percentile (M_{high}), and full width at half max (FWHM) to assess the quantity and distribution of mineralized material within the samples.

5.10 Quantitative Real-Time PCR

Total RNA was isolated using a custom CTAB method [73]. Briefly, each sample was digested with 250 μL of RNAse-free proteinase K solution 5 mg/mL, containing 5 mM $CaCl_2$. The digested samples were mixed with 500 μL of Cetyl trimethylammonium bromide (CTAB) solution (2% [w/v], 1.4 M NaCl, 20 mM EDTA, and 100 mM Tris, pH 8) containing 1% (v/v) β-mercaptoethanol. Then 500 μL of chloroform was added to each sample and centrifuged at 14,000 g for 2 min at room temperature. The upper/aqueous phase was transferred to a fresh tube and 800 μL of isopropanol (Fisher) was added to precipitate total RNA by centrifugation (14,000 g, 15 min, room temperature). The pellet was washed with 600 μL ethanol (70% v/v) and dissolved in 20 μL RNAse-free water for 15 min at 65°C. RNA purity and yield were assessed using a spectrophotometer (DS-11 FX, DeNovix), with 260/280 and 260/230 ratios over 1.8 for all samples. 300 ng of RNA from each sample was transcribed into cDNA using Qiagen Quantinova reverse transcription kits and thermal cycler (5PRIMEG/O2, Prime). Relative gene expression was studied by quantitative real-time polymerase chain reaction (qRT-PCR). The genes of interest included osteoblast and osteocyte specific genes: bone sialoprotein (BSP) and osteopontin (OPN), dentin matrix acidic phosphoprotein 1 (DMP1) and sclerostin (SOST), osteoclast specific genes: nuclear factor of activated T cell 1 (NFATC1) and osteoclast associated receptor (OSCAR), genes associated with bone resorption: Receptor Activator for Nuclear Factor κ B Ligand (RANKL) and osteoprotegerin (OPG), and genes implicated in metastasis: Parathyroid hormone-related protein (PTHrP), Interleukin 6 (IL-6), Transforming growth factor β (TGF-β) and Tumor necrosis factor alpha (TNF-α). Rplp0 and Rpl13A were used as reference genes (Table 1). qRT-PCR was carried out with 12.5 ng of cDNA per model, using a Qiagen Quantinova SYBR Green PCR kit and a Quant Studio 5 PCR machine (Applied Biosciences). The PCR was conducted with an enzyme activation step at 95°C for 2 min, and then for 40 cycles with the following steps: 5 s denaturation at 95°C and specific annealing temperatures for each primer pair (Table 1) for 18 s. Analysis of the results was done using the Pfaffl method (Pfaffl, 2001), and the results are expressed as relative quantitative changes to samples from day 0.

Table 1. List of primers employed for qRT-PCR, including sequences (5'-3') and annealing temperatures (Tm).

Gene	Forward Primer	Reverse Primer	Tm (°C)
BSP	**CGGCGATAGTTCCGAAGAGG**	**TTTCTGCATCTCCAGCCTTCT**	**56.3**
TNF-α	**CCC TCA CAC TCA GAT CAT CTT CT**	**GCT ACG ACG TGG GCT ACA G**	**52**
TGFβ-1	**ATC TAC TGC CTC TGC CCT GA**	**ACA CAT ACG AGG CGG AAA TC**	**52**
IL-6	**GAC AAC TTT GGC ATT GTG G**	**ATG CAG GGA TGA TGT TCT G**	**54.5**
OPN	**AGCAAGAAACTCTTCCAAGCAA**	**GTGAGATTCGTCAGATTCATCCG**	**55.2**
DMP1	**AAGCTAGCCCAGAGGGACAGGCAA**	**TTATCGGCGCCGGTCCCCGTAC**	**58**
SOST	**CTTCAGGAATGATGCCACAGAGGT**	**ATCTTTGGCGTCATAGGGATGGTG**	**58**
RANKL	**CCCATCGGGTTCCCATAAAG**	**AGCAAATGTTGGCGTACAGG**	**58**
OPG	**GCCACGCAAAAGTGTGGAAT**	**TTTGGTCCCAGGCAAACTGT**	**57.5**
NFATc1	**AGGGTCGAGGTGACACTAGG**	**GAGCGGAGAAACTTTGCGG**	**58**
OSCAR	**CGTTGATCCCAGGAGTCACAA**	**GTCCTGTCGCTGATACTCCA**	**57**
PTHrP	**AACCTGCTCCCAACACCAAA**	**AATGCGTCCTTAAGCTGGGC**	**58**

RPLp0	**AGATTCGGGATATGCTGTTGGC**	**TCGGGTCCTAGACCAGTGTTC**	**58.2**
Rpl13A	**TACCAGAAAGTTTGCTTACCTGGG**	**TGCCTGTTTCCGTAACCTCAAG**	**57.3**

5.11 Statistical Analysis

Statistical analyses were performed using GraphPad Prism (version 8) software. Two-way ANOVA was used for analysis of variance with Bonferroni's post-hoc tests to compare between groups. The results are displayed as mean ± standard deviation, with significance at a level of $p \leq 0.05$. Three to four replicates were analyzed for each experimental group. The experiments were repeated 3 times.

Acknowledgments: This research was funded by IRC Laureate Award Programme 2017/18, MEMETic, IR-CLA/2017/217. The authors acknowledge the facilities and scientific and technical assistance of the Centre for Microscopy and Imaging at the National University of Ireland Galway (www.imaging.nuigalway.ie). The authors would also like to acknowledge Servier Medical Art (www.servier.com) for their image bank used to produce the figures.

Author Contributions: Conceptualization, S.M.N., V.K., E.M., L.McN.; methodology, S.M.N., V.K., A.S.K.V., E.M., L.McN.; validation S.M.N. and V.K.; formal analysis, S.M.N., V.K. and A.S.K.V.; investigation, S.M.N. and V.K.; data curation, S.M.N. and V.K.; writing—original draft preparation, S.M.N. and V.K.; writing—review and editing, S.M.N., V.K., A.S.K.V., E.M., L.McN; visualization, S.M.N., V.K.; supervision, E.M., L.McN; project administration, S.M.N. and L.McN.; funding acquisition, L.McN. All authors have read and agreed to the published version of the manuscript.

Competing Interests: The authors declare no conflict of interest. The funders had no role in the design of the study; in the collection, analyses, or interpretation of data; in the writing of the manuscript, or in the decision to publish the results.

6. References

1 Mundy, G. R. Metastasis to bone: causes, consequences and therapeutic opportunities. *Nature Reviews Cancer* **2**, 584-593, doi:10.1038/nrc867 (2002).

2 Sloan, E. K. & Anderson, R. L. Genes involved in breast cancer metastasis to bone. *Cellular and Molecular Life Sciences CMLS* **59**, 1491-1502, doi:10.1007/s00018-002-8524-5 (2002).

3 Thomas, R. C. *et al.* Bone: A Fertile Soil for Cancer Metastasis. *Current Drug Targets* **18**, 1281-1295, doi:http://dx.doi.org/10.2174/1389450117666161226121650 (2017).

4 Waning, D. L. & Guise, T. A. Molecular mechanisms of bone metastasis and associated muscle weakness. *Clinical cancer research : an official journal of the American Association for Cancer Research* **20**, 3071-3077, doi:10.1158/1078-0432.CCR-13-1590 (2014).

5 Guise, T. A. Molecular mechanisms of osteolytic bone metastases. *Cancer* **88**, 2892-2898, doi:10.1002/1097-0142(20000615)88:12+<2892::Aid-cncr2>3.0.Co;2-y (2000).

6 Jin, X. & Mu, P. Targeting Breast Cancer Metastasis. *Breast Cancer (Auckl)* **9**, 23-34, doi:10.4137/BCBCR.S25460 (2015).

7 Paszek, M. J. & Weaver, V. M. The Tension Mounts: Mechanics Meets Morphogenesis and Malignancy. *Journal of Mammary Gland Biology and Neoplasia* **9**, 325-342, doi:10.1007/s10911-004-1404-x (2004).

8 Albelda, S. *et al.* Integrin Distribution in Malignant Melanoma: Association of the ??3 Subunit with Tumor Progression. *Cancer research* **50**, 6757-6764 (1990).

9 Pignatelli, M., Cardillo, M. R., Hanby, A. & Stamp, G. W. H. Integrins and their accessory adhesion molecules in mammary carcinomas: Loss of polarization in poorly differentiated tumors. *Human Pathology* **23**, 1159-1166, doi:https://doi.org/10.1016/0046-8177(92)90034-Z (1992).

553 10 Zaman, M. H. *et al.* Migration of tumor cells in 3D matrices is governed by matrix stiffness along with cell-matrix adhesion
554 and proteolysis. *Proceedings of the National Academy of Sciences of the United States of America* **103**, 10889-10894,
555 doi:10.1073/pnas.0604460103 (2006).
556 11 Suresh, S. Biomechanics and biophysics of cancer cells. *Acta biomaterialia* **3**, 413-438, doi:10.1016/j.actbio.2007.04.002 (2007).
557 12 Makale, M. Cellular mechanobiology and cancer metastasis. *Birth Defects Research Part C: Embryo Today: Reviews* **81**, 329-343,
558 doi:10.1002/bdrc.20110 (2007).
559 13 Guo, W. & Giancotti, F. G. Integrin signalling during tumour progression. *Nature Reviews Molecular Cell Biology* **5**, 816-826,
560 doi:10.1038/nrm1490 (2004).
561 14 Ingber, D. Mechanobiology and diseases of mechanotransduction. *Annals of Medicine* **35**, 564-577,
562 doi:10.1080/07853890310016333 (2003).
563 15 Walker, C., Mojares, E. & Del Río Hernández, A. Role of Extracellular Matrix in Development and Cancer Progression.
564 *International journal of molecular sciences* **19**, doi:10.3390/ijms19103028 (2018).
565 16 Fenner, J. *et al.* Macroscopic Stiffness of Breast Tumors Predicts Metastasis. *Scientific Reports* **4**, 5512, doi:10.1038/srep05512
566 (2014).
567 17 Plewes, D. B., Bishop, J., Samani, A. & Sciarretta, J. Visualization and quantification of breast cancer biomechanical
568 properties with magnetic resonance elastography. *Physics in Medicine and Biology* **45**, 1591-1610, doi:10.1088/0031-
569 9155/45/6/314 (2000).
570 18 Krouskop, T. A., Wheeler, T. M., Kallel, F., Garra, B. S. & Hall, T. Elastic Moduli of Breast and Prostate Tissues under
571 Compression. *Ultrasonic Imaging* **20**, 260-274, doi:10.1177/016173469802000403 (1998).
572 19 Ulrich, T. A., de Juan Pardo, E. M. & Kumar, S. The mechanical rigidity of the extracellular matrix regulates the structure,
573 motility, and proliferation of glioma cells. *Cancer research* **69**, 4167-4174, doi:10.1158/0008-5472.CAN-08-4859 (2009).
574 20 Paszek, M. J. *et al.* Tensional homeostasis and the malignant phenotype. *Cancer Cell* **8**, 241-254, doi:10.1016/j.ccr.2005.08.010
575 (2005).
576 21 Kostic, A., Lynch, C. D. & Sheetz, M. P. Differential matrix rigidity response in breast cancer cell lines correlates with the
577 tissue tropism. *PLoS One* **4**, e6361, doi:10.1371/journal.pone.0006361 (2009).
578 22 Page, J. M. *et al.* Matrix rigidity regulates the transition of tumor cells to a bone-destructive phenotype through integrin
579 beta3 and TGF-beta receptor type II. *Biomaterials* **64**, 33-44, doi:10.1016/j.biomaterials.2015.06.026 (2015).
580 23 Nazarian, A., von Stechow, D., Zurakowski, D., Müller, R. & Snyder, B. D. Bone Volume Fraction Explains the Variation in
581 Strength and Stiffness of Cancellous Bone Affected by Metastatic Cancer and Osteoporosis. *Calcified Tissue International* **83**,
582 368-379, doi:10.1007/s00223-008-9174-x (2008).
583 24 Kaneko, T. S., Bell, J. S., Pejcic, M. R., Tehranzadeh, J. & Keyak, J. H. Mechanical properties, density and quantitative CT
584 scan data of trabecular bone with and without metastases. *Journal of Biomechanics* **37**, 523-530,
585 doi:https://doi.org/10.1016/j.jbiomech.2003.08.010 (2004).
586 25 Canon, J. R. *et al.* Inhibition of RANKL blocks skeletal tumor progression and improves survival in a mouse model of breast
587 cancer bone metastasis. *Clin Exp Metastasis* **25**, 119-129, doi:10.1007/s10585-007-9127-1 (2008).
588 26 Thibaudeau, L. *et al.* A tissue-engineered humanized xenograft model of human breast cancer metastasis to bone. *Dis Model*
589 *Mech* **7**, 299-309, doi:10.1242/dmm.014076 (2014).
590 27 Yoneda, T., Williams, P. J., Hiraga, T., Niewolna, M. & Nishimura, R. A bone-seeking clone exhibits different biological
591 properties from the MDA-MB-231 parental human breast cancer cells and a brain-seeking clone in vivo and in vitro. *J Bone*
592 *Miner Res* **16**, 1486-1495, doi:10.1359/jbmr.2001.16.8.1486 (2001).
593 28 Khalili, P., Arakelian, A., Chen, G., Singh, G. & Rabbani, S. A. Effect of Herceptin on the development and progression of
594 skeletal metastases in a xenograft model of human breast cancer. *Oncogene* **24**, 6657-6666, doi:10.1038/sj.onc.1208790 (2005).

595 29 Harms, J. F. *et al.* A small molecule antagonist of the alpha(v)beta3 integrin suppresses MDA-MB-435 skeletal metastasis.
596 *Clin Exp Metastasis* **21**, 119-128 (2004).
597 30 Acha, A., Ruesga, M. T., Rodriguez, M. J., Martinez de Pancorbo, M. A. & Aguirre, J. M. Applications of the oral scraped
598 (exfoliative) cytology in oral cancer and precancer. *Med Oral Patol Oral Cir Bucal* **10**, 95-102, doi:10488991 [pii] (2005).
599 31 Baker, B. M. & Chen, C. S. Deconstructing the third dimension: how 3D culture microenvironments alter cellular cues. *J Cell*
600 *Sci* **125**, 3015-3024, doi:10.1242/jcs.079509 (2012).
601 32 Salamanna, F. *et al.* An in vitro 3D bone metastasis model by using a human bone tissue culture and human sex-related
602 cancer cells. *Oncotarget* **7**, 76966-76983, doi:10.18632/oncotarget.12763 (2016).
603 33 Salamanna, F. *et al.* A Human 3D In Vitro Model to Assess the Relationship Between Osteoporosis and Dissemination to
604 Bone of Breast Cancer Tumor Cells. *Journal of cellular physiology* **232**, 1826-1834, doi:10.1002/jcp.25708 (2017).
605 34 Bock, N. *et al.* In vitro engineering of a bone metastases model allows for study of the effects of antiandrogen therapies in
606 advanced prostate cancer. *Sci Adv* **7**, eabg2564, doi:10.1126/sciadv.abg2564 (2021).
607 35 Colombo, M. V. *et al.* Engineering the early bone metastatic niche through human vascularized immuno bone minitissues.
608 *Biofabrication* **13**, doi:10.1088/1758-5090/abefea (2021).
609 36 Han, W. *et al.* In vitro bone metastasis dwelling in a 3D bioengineered niche. *Biomaterials* **269**, 120624,
610 doi:https://doi.org/10.1016/j.biomaterials.2020.120624 (2021).
611 37 Choi, S. *et al.* Biofunctional matrix models reveal mineral-dependent mechanoregulation of bone metastatic breast cancer.
612 *bioRxiv*, 2022.2006.2029.498001, doi:10.1101/2022.06.29.498001 (2022).
613 38 Curtis, K. J. *et al.* Mechanical stimuli and matrix properties modulate cancer spheroid growth in three-dimensional gelatin
614 culture. *Journal of The Royal Society Interface* **17**, 20200568, doi:doi:10.1098/rsif.2020.0568 (2020).
615 39 Lynch, M. E. *et al.* In vivo tibial compression decreases osteolysis and tumor formation in a human metastatic breast cancer
616 model. *J Bone Miner Res* **28**, 2357-2367, doi:10.1002/jbmr.1966 (2013).
617 40 Fan, Y. *et al.* Skeletal loading regulates breast cancer-associated osteolysis in a loading intensity-dependent fashion. *Bone Res*
618 **8**, 9, doi:10.1038/s41413-020-0083-6 (2020).
619 41 Jansen, L. E., Birch, N. P., Schiffman, J. D., Crosby, A. J. & Peyton, S. R. Mechanics of intact bone marrow. *J Mech Behav*
620 *Biomed Mater* **50**, 299-307, doi:10.1016/j.jmbbm.2015.06.023 (2015).
621 42 Rodriguez, E. K., Hoger, A. & McCulloch, A. D. Stress-dependent finite growth in soft elastic tissues. *J Biomech* **27**, 455-467,
622 doi:10.1016/0021-9290(94)90021-3 (1994).
623 43 Ambrosi, D., Pezzuto, S., Riccobelli, D., Stylianopoulos, T. & Ciarletta, P. Solid tumors are poroelastic solids with a chemo-
624 mechanical feedback on growth. *J Elast* **129**, 107-124, doi:10.1007/s10659-016-9619-9 (2017).
625 44 Tan, S. D. *et al.* Osteocytes subjected to fluid flow inhibit osteoclast formation and bone resorption. *Bone* **41**, 745-751,
626 doi:10.1016/j.bone.2007.07.019 (2007).
627 45 You, L. *et al.* Osteocytes as mechanosensors in the inhibition of bone resorption due to mechanical loading. *Bone* **42**, 172-179,
628 doi:10.1016/j.bone.2007.09.047 (2008).
629 46 Roschger, P., Paschalis, E. P., Fratzl, P. & Klaushofer, K. Bone mineralization density distribution in health and disease. *Bone*
630 **42**, 456-466, doi:10.1016/j.bone.2007.10.021 (2008).
631 47 Verbruggen, A. S. K., McCarthy, E. C., Dwyer, R. M. & McNamara, L. M. Temporal and spatial changes in bone mineral
632 content and mechanical properties during breast-cancer bone metastases. *Bone Rep* **17**, 101597,
633 doi:10.1016/j.bonr.2022.101597 (2022).
634 48 Burke, M. *et al.* The impact of metastasis on the mineral phase of vertebral bone tissue. *J Mech Behav Biomed Mater* **69**, 75-84,
635 doi:10.1016/j.jmbbm.2016.12.017 (2017).

636 49 Parle, E. *et al.* Bone Mineral Is More Heterogeneously Distributed in the Femoral Heads of Osteoporotic and Diabetic
637 Patients: A Pilot Study. *JBMR Plus* **4**, e10253, doi:10.1002/jbm4.10253 (2020).
638 50 Zhao, F., Vaughan, T. J. & McNamara, L. M. Multiscale fluid-structure interaction modelling to determine the mechanical
639 stimulation of bone cells in a tissue engineered scaffold. *Biomech Model Mechanobiol* **14**, 231-243, doi:10.1007/s10237-014-0599-
640 z (2015).
641 51 Park, P. H., McMullen, M. R., Huang, H., Thakur, V. & Nagy, L. E. Short-term treatment of RAW264.7 macrophages with
642 adiponectin increases tumor necrosis factor-alpha (TNF-alpha) expression via ERK1/2 activation and Egr-1 expression: role
643 of TNF-alpha in adiponectin-stimulated interleukin-10 production. *J Biol Chem* **282**, 21695-21703,
644 doi:10.1074/jbc.M701419200 (2007).
645 52 Ueshima, E. *et al.* Macrophage-secreted TGF-beta1 contributes to fibroblast activation and ureteral stricture after ablation
646 injury. *Am J Physiol Renal Physiol* **317**, F52-F64, doi:10.1152/ajprenal.00260.2018 (2019).
647 53 Bray, L. J. *et al.* Three-Dimensional In Vitro Hydro- and Cryogel-Based Cell-Culture Models for the Study of Breast-Cancer
648 Metastasis to Bone. *Cancers* **10**, doi:10.3390/cancers10090292 (2018).
649 54 Wang, X. & Lin, Y. Tumor necrosis factor and cancer, buddies or foes? *Acta Pharmacol Sin* **29**, 1275-1288, doi:10.1111/j.1745-
650 7254.2008.00889.x (2008).
651 55 Burow, M. E. *et al.* Differences in susceptibility to tumor necrosis factor alpha-induced apoptosis among MCF-7 breast cancer
652 cell variants. *Cancer Res* **58**, 4940-4946 (1998).
653 56 Yoshitake, F., Itoh, S., Narita, H., Ishihara, K. & Ebisu, S. Interleukin-6 directly inhibits osteoclast differentiation by
654 suppressing receptor activator of NF-kappaB signaling pathways. *J Biol Chem* **283**, 11535-11540, doi:10.1074/jbc.M607999200
655 (2008).
656 57 Naqvi, S. M., Panadero Pérez, J. A., Kumar, V., Verbruggen, A. S. K. & McNamara, L. M. A Novel 3D Osteoblast and
657 Osteocyte Model Revealing Changes in Mineralization and Pro-osteoclastogenic Paracrine Signaling During Estrogen
658 Deficiency. *Frontiers in Bioengineering and Biotechnology* **8**, doi:10.3389/fbioe.2020.00601 (2020).
659 58 Rubin, J., Rubin, C. & Jacobs, C. R. Molecular pathways mediating mechanical signaling in bone. *Gene* **367**, 1-16,
660 doi:10.1016/j.gene.2005.10.028 (2006).
661 59 el Haj, A. J., Minter, S. L., Rawlinson, S. C., Suswillo, R. & Lanyon, L. E. Cellular responses to mechanical loading in vitro. *J*
662 *Bone Miner Res* **5**, 923-932, doi:10.1002/jbmr.5650050905 (1990).
663 60 Duty, A. O., Oest, M. E. & Guldberg, R. E. Cyclic mechanical compression increases mineralization of cell-seeded polymer
664 scaffolds in vivo. *J Biomech Eng* **129**, 531-539, doi:10.1115/1.2746375 (2007).
665 61 Baas, E., Kuiper, J. H., Yang, Y., Wood, M. A. & El Haj, A. J. In vitro bone growth responds to local mechanical strain in
666 three-dimensional polymer scaffolds. *J Biomech* **43**, 733-739, doi:10.1016/j.jbiomech.2009.10.016 (2010).
667 62 Ravichandran, A. *et al.* In vitro cyclic compressive loads potentiate early osteogenic events in engineered bone tissue. *J*
668 *Biomed Mater Res B Appl Biomater* **105**, 2366-2375, doi:10.1002/jbm.b.33772 (2017).
669 63 Sittichokechaiwut, A., Edwards, J. H., Scutt, A. M. & Reilly, G. C. Short bouts of mechanical loading are as effective as
670 dexamethasone at inducing matrix production by human bone marrow mesenchymal stem cell. *Eur Cell Mater* **20**, 45-57,
671 doi:vol020a05 [pii] (2010).
672 64 Sittichockechaiwut, A., Scutt, A. M., Ryan, A. J., Bonewald, L. F. & Reilly, G. C. Use of rapidly mineralising osteoblasts and
673 short periods of mechanical loading to accelerate matrix maturation in 3D scaffolds. *Bone* **44**, 822-829,
674 doi:10.1016/j.bone.2008.12.027 (2009).
675 65 Negishi-Koga, T. *et al.* Suppression of bone formation by osteoclastic expression of semaphorin 4D. *Nat Med* **17**, 1473-1480,
676 doi:10.1038/nm.2489 (2011).

66 Soki, F. N., Park, S. I. & McCauley, L. K. The multifaceted actions of PTHrP in skeletal metastasis. *Future Oncol* **8**, 803-817, doi:10.2217/fon.12.76 (2012).

67 Wu, Q., Zhou, X., Huang, D., Ji, Y. & Kang, F. IL-6 Enhances Osteocyte-Mediated Osteoclastogenesis by Promoting JAK2 and RANKL Activity In Vitro. *Cellular physiology and biochemistry : international journal of experimental cellular physiology, biochemistry, and pharmacology* **41**, 1360-1369, doi:10.1159/000465455 (2017).

68 Yoneda, T. *et al.* Actions of bisphosphonate on bone metastasis in animal models of breast carcinoma. *Cancer* **88**, 2979-2988, doi:https://doi.org/10.1002/1097-0142(20000615)88:12+<2979::AID-CNCR13>3.0.CO;2-U (2000).

69 Bacabac, R. G. *et al.* Nitric oxide production by bone cells is fluid shear stress rate dependent. *Biochem Biophys Res Commun* **315**, 823-829, doi:10.1016/j.bbrc.2004.01.138 (2004).

70 Mullender, M. G. *et al.* Release of nitric oxide, but not prostaglandin E2, by bone cells depends on fluid flow frequency. *J Orthop Res* **24**, 1170-1177, doi:10.1002/jor.20179 (2006).

71 Haugh, M. G. *et al.* Temporal and spatial changes in cartilage-matrix-specific gene expression in mesenchymal stem cells in response to dynamic compression. *Tissue Eng Part A* **17**, 3085-3093, doi:10.1089/ten.tea.2011.0198 (2011).

72 Freeman, F. E., Haugh, M. G. & McNamara, L. M. An in vitro bone tissue regeneration strategy combining chondrogenic and vascular priming enhances the mineralization potential of mesenchymal stem cells in vitro while also allowing for vessel formation. *Tissue Eng Part A* **21**, 1320-1332, doi:10.1089/ten.TEA.2014.0249 (2015).

73 Köster, N. *et al.* Single-Step RNA Extraction from Different Hydrogel-Embedded Mesenchymal Stem Cells for Quantitative Reverse Transcription-Polymerase Chain Reaction Analysis. *Tissue Eng Part C Methods* **22**, 552-560, doi:10.1089/ten.TEC.2015.0362 (2016).

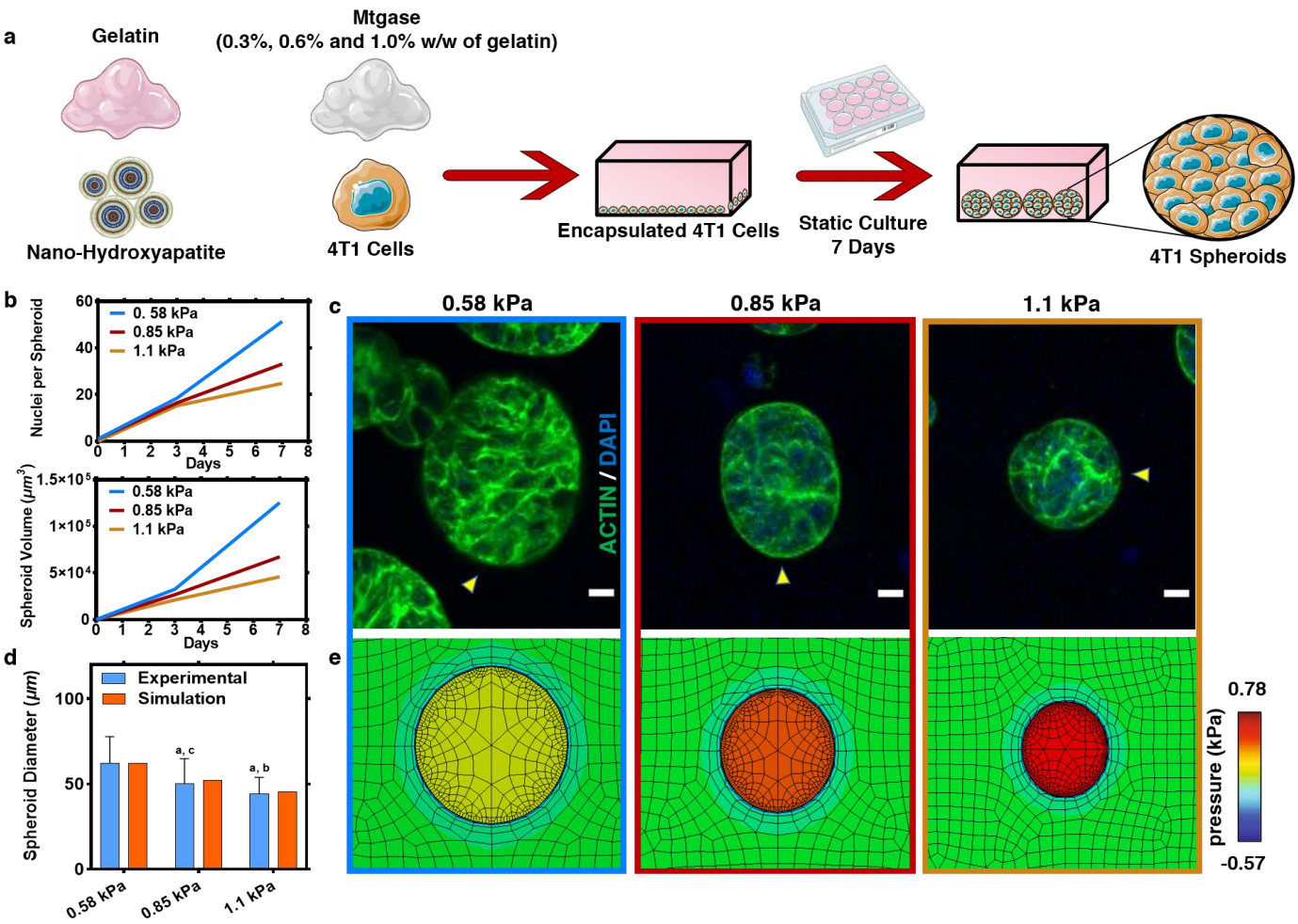

Figure 1: 4T1 mammary carcinoma cells encapsulated in gelatin hydrogels of different compression moduli (0.58 kPa, 0.85 kPa and 1.1 kPa) form spheroids whose growth is sensitive to stress imposed by the hydrogels. **a**, Schematic of the process of encapsulation of 4T1 cells in single suspension within gelatin-transglutaminase hydrogels and static culture and growth of tumor cells into spheroids. **b**, Nuclei per tumor spheroid and spheroid volume over time across three compression moduli. **c**, fluorescently stained 4T1 spheroids (arrow) within the hydrogels for Actin (green) and Dapi (blue) at day 7 (scale bar: 10 µm). **d,** Comparison of tumor spheroids in the hydrogels at day 7 of culture with results of simulation from computational tumor growth model within the hydrogels of 0.58 kPa, 0.85 kPa and 1.1 kPa compression moduli. **e**, Computational model simulation of spheroid growth within the hydrogels (represented by the green background) the resulting stresses that develop. #, a, b, c: significance compared to 4T1 monoculture, 0.58 kPa, 0.85 kPa and 1.1 kPa, respectively.

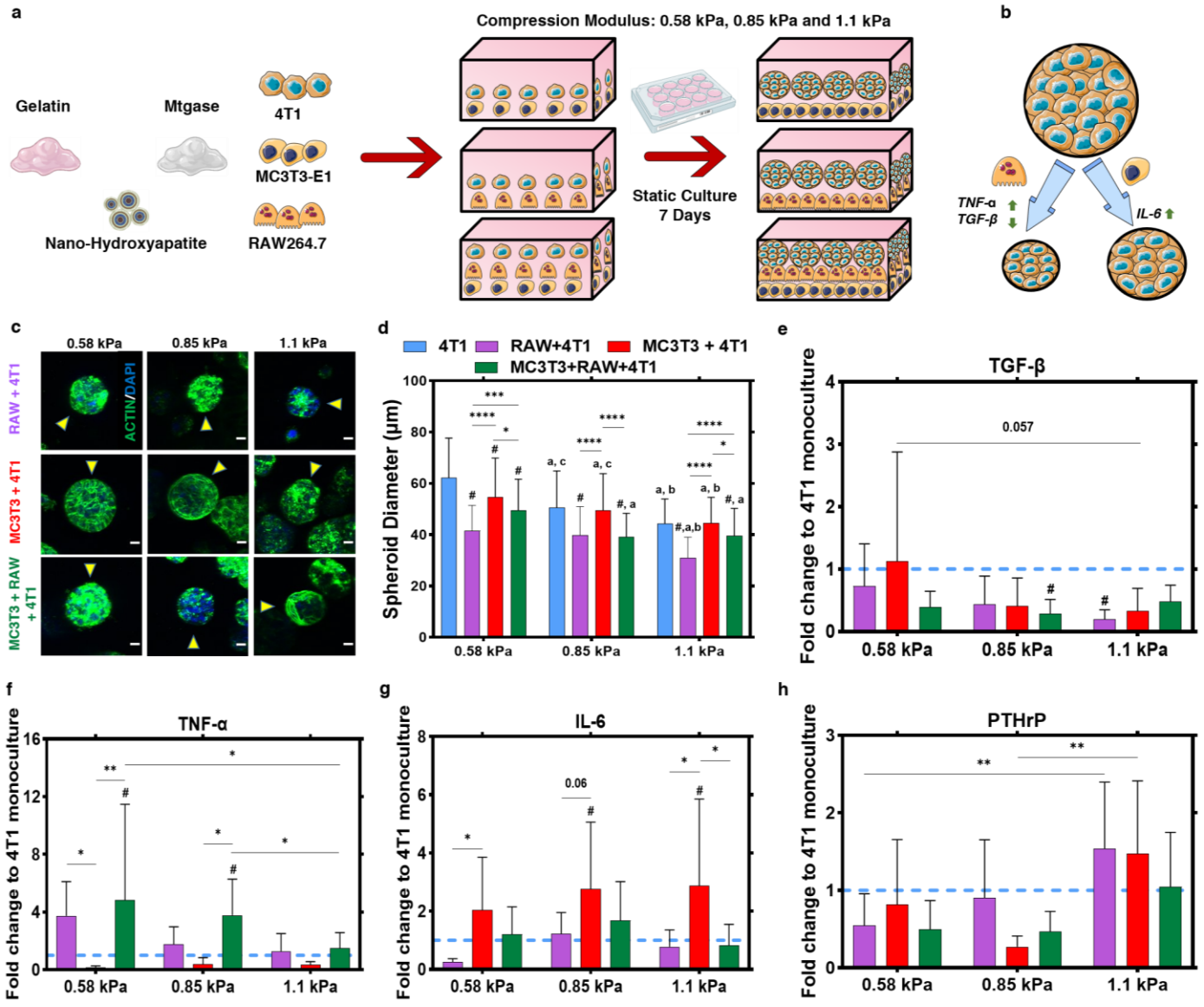

Figure 2: Inclusion of bone cells in culture with 4T1 cells in a co-culture and tri-culture configuration: Osteoclasts have an inhibitory effect on 4T1 spheroid growth which is partially mitigated by osteoblasts. a, Schematic of the process of encapsulation RAW264.7 (Osteoclast Precursors) and MC3T3-E1 (Osteoblast) with 4T1 cells in co-culture and tri-culture configurations within gelatin-transglutaminase hydrogels and static culture and growth of tumor cells into spheroids. **b,** Schematic depicting the effect of individual bone cells on the tumor spheroid. **c**, fluorescently stained 4T1 spheroids (yellow arrows) within the hydrogels for Actin (green) and Dapi (blue) at day 7 (scale bar: 10 µm) in the co-culture and tri-culture configuration with bone cells. **d**, Quantification of the 4T1 spheroid size. **e-h**, qRT-PCR analysis for, TGF-β, TNF-α, IL-6 and PTHrP. #, a, b, c: significance compared to 4T1 monoculture, 0.58 kPa, 0.85 kPa and 1.1 kPa, respectively *: $p \leq 0.05$, **: $p \leq 0.01$, ***: $p \leq 0.001$, ****: $p \leq 0.0001$.

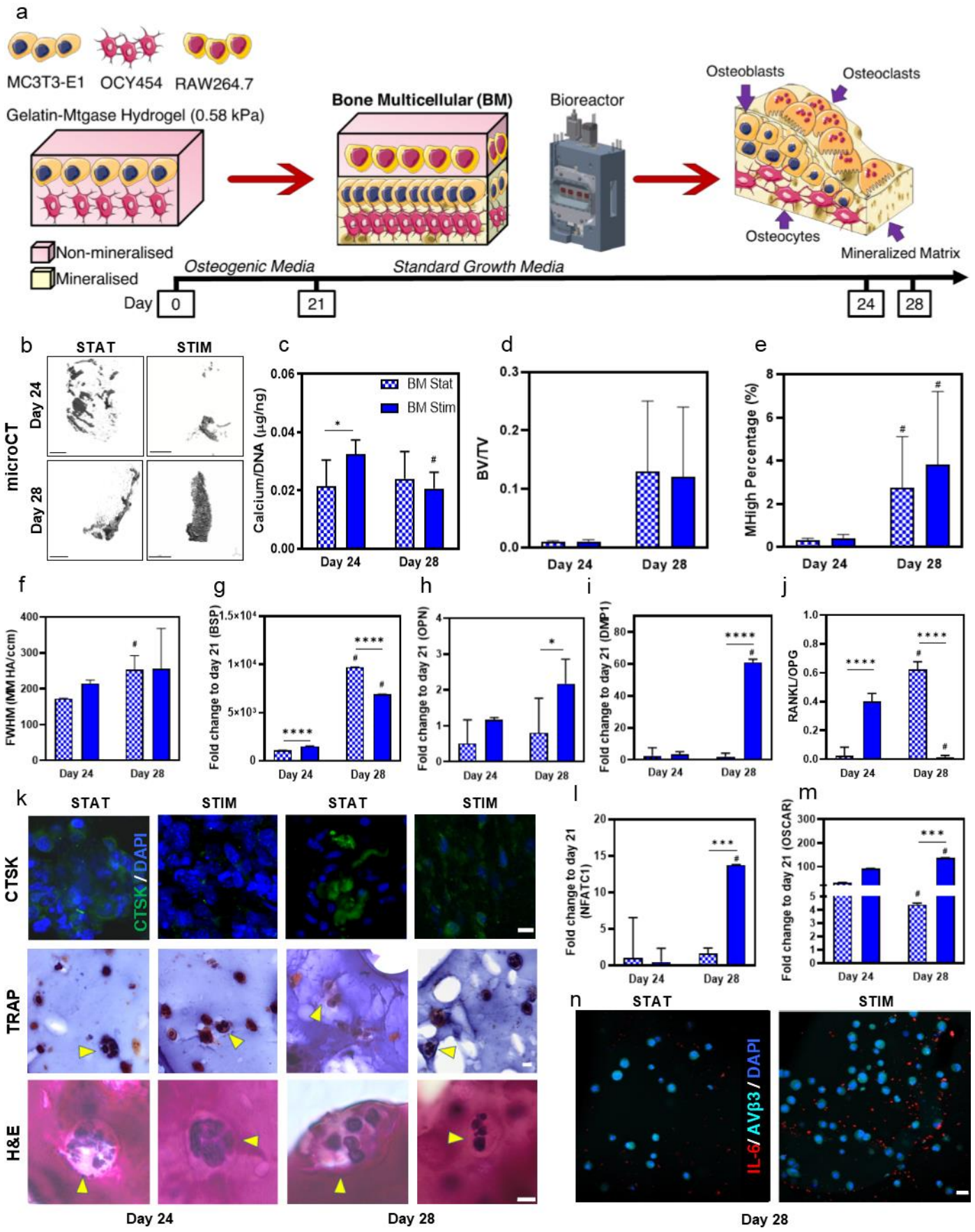

Figure 3: Bone Multicellular (BM) model have mineral deposits, osteoblastic activity and the presence of active osteoclasts in them. a, Schematic of the timeline and the process of encapsulation of OCY 454 and MC3T3-E1 cells

within gelatin-transglutaminase hydrogels followed by culture in osteogenic media for 3 weeks followed by the addition of a layer of hydrogel encapsulating RAW264.7 cells and the application of mechanical compression for 7 days. **b**, Micro-CT analysis of the models (scale bar: 1 mm). **c**, Calcium content in the models. **d**, Bone-like mineral volume fraction (BV/TV). **e**, MHigh percentage. **f**, FWHM. **g**, qRT-PCR analysis for BSP2 expression in the BM model. **h**, qRT-PCR analysis for OPN expression. **i**, qRT-PCR analysis for DMP1 expression. **j,** RANKL/OPG. **k**, Immunofluorescence staining for CTSK (scale bar: 10 µm) and Histology for TRAP (scale bar: 20 µm) and H&E (scale bar: 10 µm) in the BM model **l**, qRT-PCR analysis for NFATC1 expression. **m**, qRT-PCR analysis for OSCAR expression. **n**, Immunofluorescence for IL-6 and Avβ3 day 28 in the BM model (scale bar: 20 µm). #: significance compared to day 24, *: $p \leq 0.05$, **: $p \leq 0.01$, ***: $p \leq 0.001$, ****: $p \leq 0.0001$.

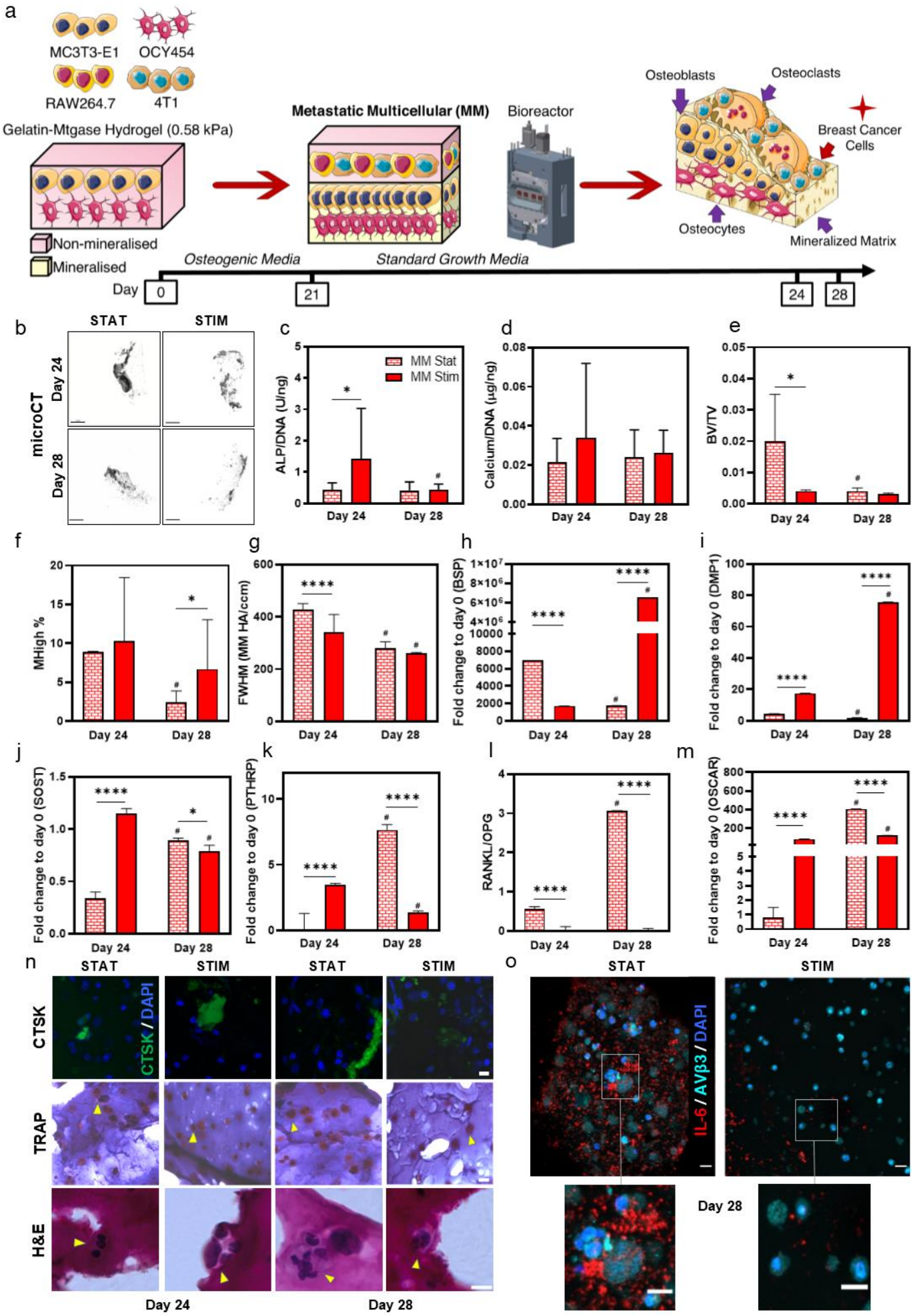
a
MC3T3-E1
OCY454
RAW264.7
4T1
Gelatin-Mtgase Hydrogel (0.58 kPa)
Non-mineralised
Mineralised
Metastatic Multicellular (MM)
Bioreactor
Osteoblasts
Osteoclasts
Breast Cancer Cells
Osteocytes
Mineralized Matrix
Osteogenic Media
Standard Growth Media
Day
0
21
24
28
b
STAT
STIM
microCT
Day 24
Day 28
c
MM Stat
MM Stim
ALP/DNA (U/ng)
d
Calcium/DNA (µg/ng)
e
BV/TV
f
MHigh %
g
FWHM (MM HA/ccm)
h
Fold change to day 0 (BSP)
i
Fold change to day 0 (DMP1)
j
Fold change to day 0 (SOST)
k
Fold change to day 0 (PTHRP)
l
RANKL/OPG
m
Fold change to day 0 (OSCAR)
n
CTSK
TRAP
H&E
CTSK / DAPI
o
IL-6 / AVβ3 / DAPI

Figure 4: Metastatic Multicellular model exhibit osteolytic metastatic response which is attenuated under mechanical compression. a, Schematic of the timeline and the process of encapsulation of OCY 454 and MC3T3-E1 cells within gelatin-transglutaminase hydrogels followed by culture in osteogenic media for 3 weeks followed by the addition of a layer of hydrogel encapsulating RAW264.7 and 4T1 cells and the application of mechanical compression for 7 days. **b**, Micro-CT analysis of the models (scale bar: 1 mm). **c**, ALP activity. **d**, Calcium content in the models. **e**, Bone-like mineral volume fraction (BV/TV). **f**, MHigh percentage. **g**, FWHM. **h**, qRT-PCR analysis for BSP expression in the MM model. **i**, qRT-PCR analysis for DMP1 expression. **j**, qRT-PCR analysis for SOST expression. **k**, qRT-PCR analysis for PTHrP expression. **l**, RANKL/OPG. **m**, qRT-PCR analysis for OSCAR expression. **n**, Immunofluorescence staining for CTSK (scale bar: 10 µm) and Histology for TRAP (scale bar: 20 µm) and H&E (scale bar: 10 µm) in the MM model. **o**, Immunofluorescence for IL-6 and AVβ3 day 28 in the MM model (scale bar: 20 µm). #: significance compared to day 24, *: $p \leq 0.05$, **: $p \leq 0.01$, ***: $p \leq 0.001$, ****: $p \leq 0.0001$.

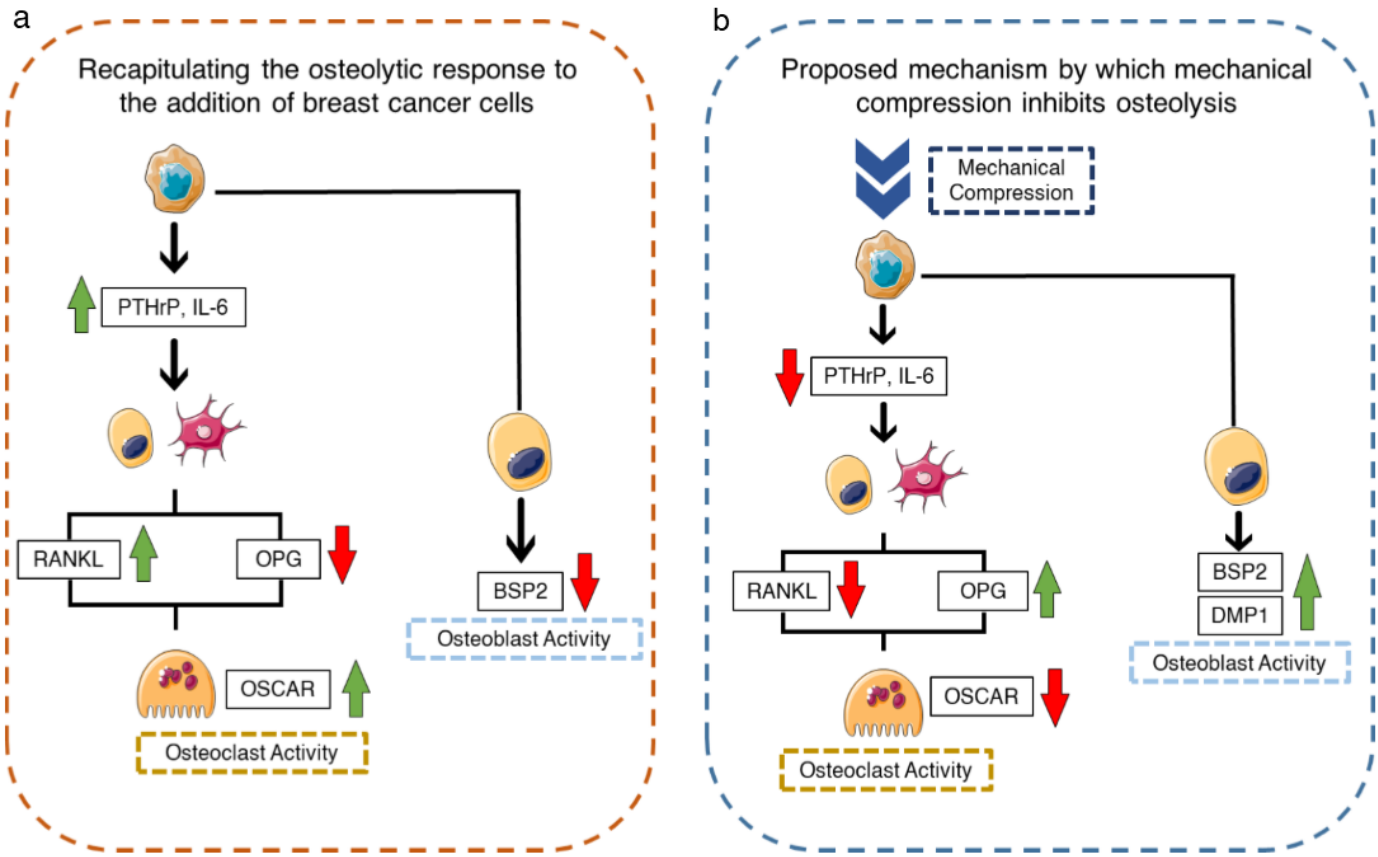

Figure 5: (a) Recapitulating the osteolytic response to the addition of breast cancer cell using the 3D in vitro multicellular mineralized model. Breast cancer cells secrete biochemical factors that stimulate osteoclastogenesis through the RANKL/OPG pathway and downregulate osteoblastic activity. (**b**) **Proposed mechanism by which mechanical compression inhibits this osteolytic response.** Mechanical compression leads to a reduction in the expression of osteolytic factors, which in turn leads to a reduction in expression of the factors supporting osteoclastogenesis, while genes associated with osteoblast activity are upregulated.